EES Batteries

PAPER

View Article Online
View Journal

Cite this: DOI: 10.1039/d6eb00045b

Nonuniform charging and phase front instability in nickel (oxy)hydroxide thin-film electrodes

Aleksandr Kurilovich, †[a] Avihay Ben Shitrit, †[a] David S. Ellis, †[a] Nadav Port, [b] Nir Gavish, [c] Arik Yochelis *[b,d] and Avner Rothschild *[a,e,f]

Some battery electrodes undergo phase transitions during ion insertion and extraction in electrochemical cycling. These transitions often limit electrode capacity, rate performance, and cycle life, making them critical in electrochemical energy storage. Work in this area has largely centered on phase propagation dynamics at the level of individual particles, thereby reinforcing the prevailing paradigm that macroscopic electrode behavior directly arises from the microscopic dynamics of its constituent particles. Yet this paradigm disregards emergent macroscopic effects and self-organization that can shape electrode behavior in complex and non-trivial ways. Here, we uncover an emergent effect that drives lateral propagation – perpendicular to the applied driving force – of a millimeter-scale phase front between charged NiOOH and discharged $Ni(OH)_2$ during the charging of thin-film (~50 nm) nickel (oxy)hydroxide electrodes. We introduce a novel mechanistic explanation for this counterintuitive behavior, attributing it to long-range coulombic interactions between charged regions at the phase front. These interactions trigger planar front instability, akin to the forces that drive phase separation and self-organization in bulk heterojunction organic photovoltaic cells. Thus, this study challenges the fundamental understanding of electrochemical phase transitions in ion insertion electrodes, particularly in thin-film systems, uncovering a new perspective on how the delicate interplay between charging rate and charging uniformity governs battery performance.

Received 27th February 2026,
Accepted 2nd March 2026

DOI: 10.1039/d6eb00045b

rsc.li/EESBatteries

Broader context

Electrochemical phase transitions are fundamental to the operation of battery electrodes, electrocatalysts, and electrochromic devices. Traditionally, these transitions have been understood through the behavior of micrometer-scale particles within the electrode, while large-scale collective phenomena have been largely overlooked. Yet such emergent dynamics could strongly influence electrode function—echoing Gerhard Ertl's theory of reaction complexity. This prompts a central question: *could similar forms of self-organization arise in cycling battery electrodes?* To explore this, we visualized phase transitions in nickel (oxy)hydroxide thin film electrodes. Their color change—from pale $Ni(OH)_2$ to dark NiOOH—enabled real-time optical imaging of phase evolution. Remarkably, we found that the transition evolves through lateral propagation of macroscopic phase front across the electrode, perpendicular to the applied field, rather than uniformly through the material as previously assumed. This reveals a fundamental symmetry-breaking mechanism that produces nonuniform charging—regions that overcharge while others remain uncharged—leading to premature oxygen evolution. The symmetry-breaking mechanism is routed in electrostatic interactions between oppositely charged regions that amplify perturbations along the phase front, giving rise to counter-propagating waves driven by both external and internal fields. These insights provide a new framework for understanding dynamic electrode behavior and guiding improved cycling strategies to enhance battery performance.

Introduction

Electrochemical phase transitions are pervasive in energy materials such as rechargeable battery electrodes,[1–4] electrocatalysts for water electrolysis,[5] and electrochromic windows.[6] They occur during electrochemical reactions in which small ions, such as Li^+ or H^+, are inserted (or extracted) into (from) the electrode. The inserted ions are accompanied by electrons that reduce transition metal cations in the electrode. The difference in the ionic radii of the reduced *vs.* oxidized cations results in a local distortion, whereby large enough distortions trigger topochemical phase transitions.[3]

[a]*Department of Materials Science and Engineering, Technion – Israel Institute of Technology, Haifa, Israel. E-mail: avnerrot@technion.ac.il*
[b]*Swiss Institute for Dryland Environmental and Energy Research, Blaustein Institutes for Desert Research, Ben-Gurion University of the Negev, Sede Boqer Campus, Midreshet Ben-Gurion 8499000, Israel. E-mail: yochelis@bgu.ac.il*
[c]*Department of Mathematics, Technion – Israel Institute of Technology, Haifa, Israel*
[d]*Department of Physics, Ben-Gurion University of the Negev, Be'er Sheva 8410501, Israel*
[e]*The Grand Technion Energy Program (GTEP), Technion – Israel Institute of Technology, Haifa, Israel*
[f]*The Stewart and Lynda Resnick Sustainability Center for Catalysis (RSCC), Technion – Israel Institute of Technology, Haifa, Israel*
†These authors contributed equally.

The distinct electronic properties of the reduced and oxidized phases affect functional electrode properties such as electrical conductivity (electronic and ionic), color, electrocatalytic activity and charge storage capacity.[4,7] These properties depend on the phase distribution within the electrode. Therefore, a central challenge is to understand the spatiotemporal dynamics of electrochemical phase transitions in order to predict and control phase propagation through operational parameters, such as charging rate, and thereby optimize battery performance.[7,8] To this end, researchers have harnessed a broad array of operando imaging methods to visualize the spatiotemporal progression of phase transitions during operation.[9,10] However, most studies have focused on phase propagation dynamics at the level of single particles or small particle clusters, using advanced microscopic methods with nanometer-scale resolution.[11–13] For example, Lim *et al.* used X-ray microscopy to visualize phase transitions in single Li_xFePO_4 particles over multiple lithiation and delithiation cycles.[11] They observed a shift from a spatially nonuniform biphasic transition at low lithiation and delithiation rates to a uniform solid-solution-like behavior at high lithiation rates, and phase separation into biphasic domains upon spontaneous relaxation to the equilibrium state. Their results align with earlier hypotheses regarding the origin of voltage hysteresis and the fast-charging capability of Li_xFePO_4 electrodes.[14,15] Collectively, these studies reinforce the prevailing paradigm that the macroscopic behavior of electrodes during cycling directly mirrors the microscopic dynamics of their constituent particles.[16]

Consequently, little attention has been paid to macroscopic emergent phenomena that could influence electrode behavior in nontrivial ways,[17] such as in the case of catalytic CO oxidation on Rh electrodes,[18] which inspired Gerhard Ertl to develop the theory of self-organization and complexity in catalytic reactions, work that earned him the 2007 Nobel Prize in Chemistry. Seeking to bridge this gap, in this work we investigate the spatiotemporal dynamics of electrochemical phase transitions in nickel (oxy)hydroxide electrodes at the macroscopic scale. These electrodes are widely used in rechargeable alkaline batteries,[19] alkaline and decoupled water electrolyzers,[20,21] and supercapacitors.[22] They present electrochromism, changing color from light green (nickel hydroxide, $Ni(OH)_2$) to dark grey (nickel oxyhydroxide, NiOOH) during charging (oxidation), and reverses during discharging (reduction).[23,24] This color change enables monitoring the progression of the phase transition between $Ni(OH)_2$ and NiOOH by simple optical imaging, which is suitable for observing macroscopic objects larger than ~1 μm and provides a large field of view that covers the entire electrode area. Another useful merit of this method is fast video recording that enables tracking the phase propagation in real time.

Electrochemical phase transitions in nickel (oxy)hydroxide electrodes have been studied since the 1950's. Glemser and Einerhand reported the structure of different phases of nickel (oxy)hydroxide;[25,26] Conway and Bourgault pioneered the electrochemistry of nickel (oxy)hydroxide electrodes during anodic polarization;[27] and Bode *et al.* presented a diagram that illustrates the transitions from one phase to another upon chemical and electrochemical reactions.[28] The emerging pattern of the phase transition was examined by Briggs and Fleischmann, who presented a cross-section photograph of a partially charged electrode that displayed a planar boundary between the oxidized and reduced phases, based on which they argued that "*the boundary moves progressively through the layer as it is charged, roughly parallel to the metal support*".[29] Based on these and other studies, Huggins *et al.* suggested that the charge and discharge mechanism of nickel (oxy) hydroxide electrodes involves proton diffusion through an outer layer of $Ni(OH)_2$ from/to the $Ni(OH)_2$/NiOOH interphase boundary (aka phase front), where the electrochemical reaction $Ni(OH)_2 \rightleftharpoons NiOOH + H^+ + e^-$ takes place.[30] The protons released/consumed at the phase front travel to/from the surface where they react with hydroxide ions from the alkaline electrolyte, $H^+ + OH^- \rightleftharpoons H_2O$. As the reaction progresses, the phase front propagates through the layer as illustrated in Fig. 1(a). When it reaches the surface (during charging), the NiOOH phase gets in contact with the electrolyte and gives rise to oxygen evolution since NiOOH has strong electrocatalytic activity for the oxygen evolution reaction (OER), especially in the presence of iron impurities.[31,32] Once this happens, oxygen evolution competes with further charging of the electrode.[33]

If the phase front propagates uniformly as a planar front through the electrode, as illustrated in Fig. 1(a), oxygen evolution would begin after most of the electrode has been charged, when the poorly conducting $Ni(OH)_2$ phase no longer separates the electrocatalytic NiOOH phase from the electrolyte. However, if the phase transition occurs nonuniformly, such that some regions in the electrode are charged faster than other regions, premature oxygen evolution may occur, competing with charging the remaining uncharged regions. Thus, nonuniform charging may restrict nickel (oxy)hydroxide electrodes from reaching their full capacity.[33–35] This may also apply to other electrodes in aqueous and non-aqueous electrolytes, where other parasitic reactions may occur.[36] Remarkably, this phenomenon has remained largely unexplored, even though it could significantly impair battery performance.

To explore this hypothesis, we visualize the phase propagation in translucent thin-film nickel (oxy)hydroxide electrodes during cyclic voltammetry (CV) and galvanostatic charge and discharge (GDC) cycles. Exploiting the optical contrast between $Ni(OH)_2$ and NiOOH, we use a portable digital microscope that can be readily placed in front of the electrode to video record the pattern of color change during CV and GDC cycling (Fig. S1). The electrodes comprise a thin layer (~50 nm) of nickel (oxy)hydroxide on a transparent conductive substrate (ITO- or FTO-coated glass) that enables imaging through the electrode. If the phase transition progresses uniformly across the electrode by a planar front that propagates through the nickel (oxy)hydroxide layer from the substrate to the surface, as suggested by Huggins[30] (Fig. 1(a)), it would result in a gradual change in color across the entire electrode,

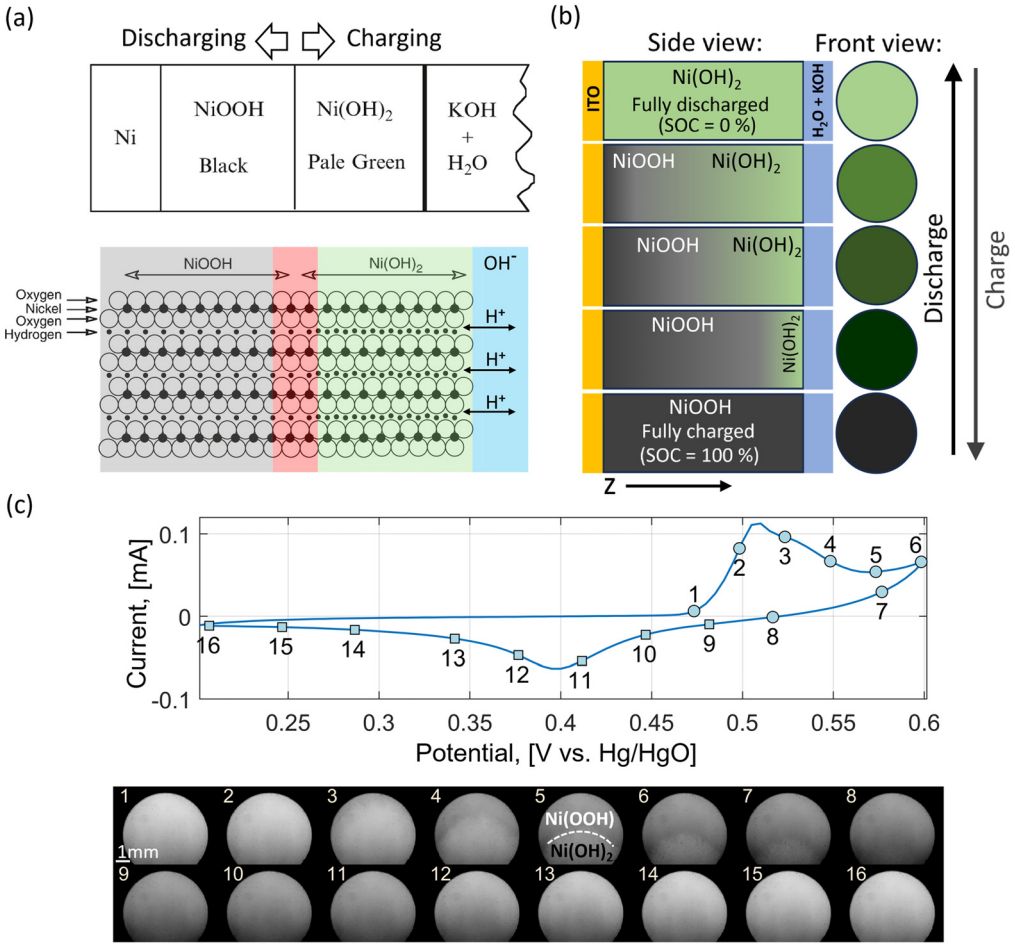

Fig. 1 Uniform *vs.* nonuniform charging. (a) Schematic side view illustration of a uniform phase transition between $Ni(OH)_2$ (green) and NiOOH (grey) that gives rise to planar phase front (red) propagation through the nickel (oxy)hydroxide layer. Adapted from ref. 29. (b) Left: Side view depiction of hypothetical gradual color changes through the layer, along the *z* direction, as the phase front propagates from the substrate side towards the electrolyte side. Right: The corresponding average color as viewed normal to the *z* direction (*i.e.*, in the *x*–*y* plane), assuming planar front propagation along the *z* direction. (c) Top: A typical CV cycle of $Ni(OH)_2$ electrode SIL1, with numbered points sampled along the anodic (circles) and cathodic (squares) parts of the cycle. Bottom: Video frames, extracted from Video S1, corresponding to the times of each of the above points, converted to gray scale images and enhanced for visual contrast.

as illustrated in Fig. 1(b). It is noted that a gradual change in color occurring uniformly across the electrode would also be expected for an ensemble of microscopic particles that transform simultaneously from one phase to another, unless there are specific interactions between the particles that give rise to self-organization at a macroscopic length scale, or some other macroscopic effects that have not been accounted for.

Strikingly, we observed *lateral* propagation of the darkened, charged phase (NiOOH) that expands as a propagating wave characterized by a single, macroscopic interface (*i.e.*, a phase front) that traverses the electrode from one side to the other, perpendicularly to the applied driving force, as demonstrated in Fig. 1(c). This characteristic feature clearly distinguishes a front-controlled transformation governed by the propagation of a phase front from classical phase transformations that proceed *via* nucleation and growth of multiple nuclei, each generating its own boundary. The rest of the article presents experimental evidence of macroscopic lateral front propagation under various conditions and across different electrodes. We analyze the characteristics of lateral front propagation and present a theoretical framework that can explain the symmetry-breaking mechanism behind this counterintuitive phenomenon—a process that could critically limit battery performance.

Results and discussion

To observe the spread of charged (darkened) state in the whole of the electrode by a two-dimensional image, the color change from uncharged $Ni(OH)_2$ (light) to fully charged NiOOH (dark) should ideally match with the dynamic range of the camera. Considering that the optical absorption coefficient (α) through the nickel (oxy)hydroxide layer increases in proportion to the

amount of the material that is charged, and that the sensitivity of most cameras is linear, the above condition would be met if the light transmission through the electrode, $e^{-\alpha l_z}$, could be linearized. In other words, the layer thickness l_z should be smaller than the light penetration length α^{-1}. This could be achieved with thinfilm electrodes. This, in turn, simplifies data analysis and requires minimal image processing. Another requirement is layer uniformity, to avoid spurious structural defects that could cause uneven color changes across the electrode. Accordingly, we deposited a uniform thin layer (~50 nm) of nominally undoped $Ni(OH)_2$ on transparent indium tin oxide (ITO) coated glass substrates by successive ionic layer adsorption and reaction (SILAR), a layer-by-layer deposition technique that is known for producing uniform films.[37] Based on quantitative analysis of the optical properties of two electrodes, SIL3 and SIL4, linearization of the Beer–Lambert decay of light intensity penetrated through these samples was found to introduce optical errors of less than 4.6% and 8.8%, respectively, validating that the trailing error in our analysis does not compromise the robustness of our conclusions. After deposition, electrode formation (aka activation) was performed by repeating 200 CV cycles between 0.2 and 0.54 V *vs.* Hg/HgO at a sweep rate of 2 mV s^{-1} in 1 M KOH aqueous electrolyte, to stabilize its charge capacity.

Characterizations of microstructure and surface morphology, layer thickness and uniformity, chemical and phase composition, and impurity distribution using a variety of SILAR deposited samples (SIL1–SIL4), are presented in SI Sections S2–S5. Although the electrodes were not intentionally doped, they were found to incorporate iron impurities from the electrolyte. This is indicated by the early onset of OER in their CV curves, which is associated with the presence of iron in the electrolyte,[38,39] and confirmed by Rutherford backscattering spectrometry (RBS) measurements before and after electrode formation (SI Section S3).

After electrode formation, the electrodes were video recorded by a portable digital microscope during CV and GDC cycles, with the microscope positioned to image the sample as depicted in Fig. S1, as it underwent electrochemical oxidation (charging) and reduction (discharging). The apparatus and procedure are described in the Experimental section. Contrary to the expected uniform gradual color change indicative of laterally uniform charging, as envisioned in Fig. 1(b), the charging evolved nonuniformly as a laterally propagating wave with a continuous front between the pale $Ni(OH)_2$ and dark Ni(OOH) phases on a scale of millimeters, as shown in Fig. 1(c) for electrode SIL1. The discharge was observed to occur uniformly. While our focus here is on SILAR-deposited $Ni(OH)_2$ electrodes as discussed above, we also observed qualitatively similar behavior in electrodes fabricated by electrochemical deposition, see ED1 sample featured in Fig. S2, and ED2 sample in Fig. S3, and corresponding Videos S2 and S3. To rule out possible edge effects arising from the O-ring seal of the electrochemical cell (Fig. S1), we repeated the measurement with electrode SIL2, prepared by the same SILAR method, which was freely immersed in a glass beaker, with the result that it likewise exhibited lateral front propagation, shown in Fig. S4 and corresponding Video S4. This relatively large-size sample was used for phase analysis by XRD, microstructure characterizations by TEM and position-dependent thickness measurements by optical reflectometry and impurity distribution by ToF-SIMS, see SI Sections S2–S5. As can be seen in Fig. S17, the thickness variations across the sample did not correlate with the darkness variations as the phase front propagated during CV cycling. Likewise, iron impurity variations did not correlate with the phase front propagation (SI Section S5).

Both CV, as shown above, and GDC measurements can drive lateral front propagation. GDC allows precise control of the amount of charge passed per unit time, *i.e.*, the current, and is thus convenient for analysis and modelling the spatio-temporal characteristics of the nonuniform charging. In addition, the transition between the charging regimes of sole electrode oxidation and mixed oxidation with competing OER can be more clearly detected by monitoring the potential profile at a constant current.[33] Fig. 2(a) and (b) show potential *versus* time curve and video frames (from Video S5) during galvanostatic charging of electrode SIL3. The time range between the initial transient (point 1 in Fig. 2(a)) and the onset of the potential plateau (point 4) corresponds to a process of ideal charging without competing oxygen evolution.[33] As the electrode continues to charge, the potential will reach a level sufficient to initiate the OER, diverting a portion of the current from charging $Ni(OH)_2$ to NiOOH to oxidizing water and evolving oxygen, thus slowing down the charging, and ultimately saturating the potential.[33,40] This latter region, so-called the

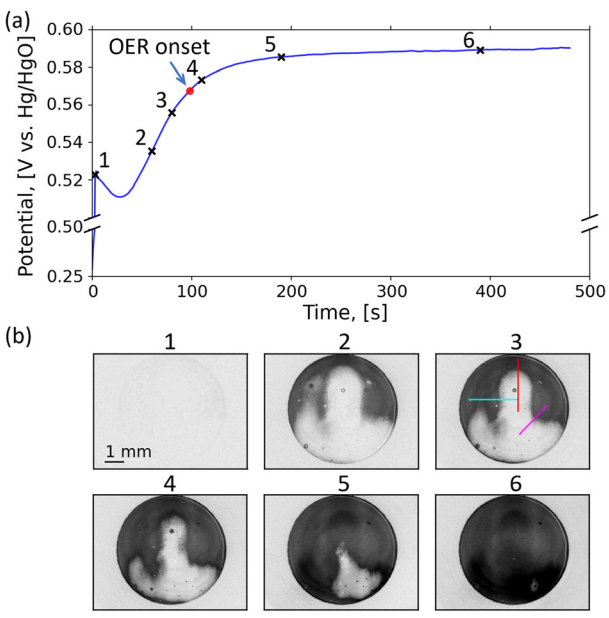

Fig. 2 Galvanostatic charging. (a) Potential *vs.* time chronopotentiometry curve for galvanostatic charging of $Ni(OH)_2$ electrode SIL3 at a constant current of 20 μA (71.4 μA cm^{-2}), with numbered points sampled in panel (b). (b) Gray scale video frames (from Video S5) corresponding to the numbered points in panel (a), after subtraction of the first frame, with display enhanced for optimal contrast without oversaturation.

potential plateau region, corresponds to oxygen evolution at a constant current, for the most part. In Fig. 2(a) we marked the onset of oxygen evolution between points 3 and 4. The video frames captured at times corresponding to the labelled points in the charging curve are shown in Fig. 2(b), after subtracting the initial frame from the images. The transition between frames 1 and 2 shows initial nucleation and further charging of the top region of the electrode (Video S5), where much of the charging takes the form of increased darkening of an already-darkened region that has been established relatively soon in the process, which we assign to 'filling out' of remaining uncharged local spots. The next stage of the charging process is expansion of the charged region like a propagating wave, as observed in frames 2–5 in Fig. 2(b), which is largely complete in frame 6, where the whole area is charged and subsequently does not darken further.

To analyze the spatiotemporal dynamics of the phase front propagation, we take several cuts along the observed propagation directions shown as colored lines on frame 3 in Fig. 2(b). These include a vertical (red) cut and horizontal (cyan) cut which are perpendicular to their respective local phase fronts, as well as a diagonal cut (magenta) crossing a rounded corner. Charge profile progression along the respective cuts, extracted from the locally-averaged darkening of the grayscale pixels along the cut relative to the discharged state, $\langle \Delta \bar{b} \rangle$ where $\bar{b}$ is the darkness of the pixel (see SI Section S6 and Experimental section for details), are plotted in Fig. 3(a)–(c) for charging times corresponding to frames 2–4 in Fig. 2(b). A salient feature in these profiles is that the width of the phase fronts, over which the darkness drops continuously from its high value to its low value, is of the order of 1 mm. Remarkably, these widths are maintained as the phase front propagates along the respective cuts.

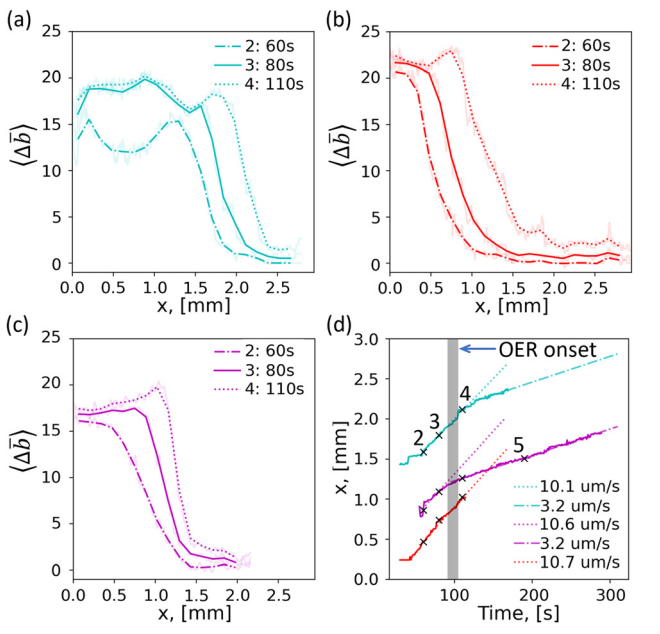

Fig. 3 Front propagation velocity. Spatial profiles of pixel darkness change in SIL3 electrode, plotted at times of 60, 80, and 110 s during galvanostatic charging at a constant current of 20 μA (71.4 μA cm^{-2}), along the (a) horizontal, (b) vertical, and (c) diagonal cuts, respectively, drawn in Fig. 2(b). (d) Central position of the phase front *vs.* time, for the different propagation directions, with matching colors to panels (a)–(c). The approximate time of the onset of oxygen evolution is indicated by the vertical grey line.

The front propagation velocity in these directions is obtained by plotting the central position of the respective phase fronts as a function of time in Fig. 3(d). The approximate time of the onset of oxygen evolution, marked by the red dot in Fig. 2(a), is indicated as a vertical grey line in Fig. 3(d). The phase fronts along all directions propagate at very similar velocities of about 10 to 11 μm s^{-1}. After some of the current is diverted to the OER, the front propagation velocities decrease to about 3 μm s^{-1}, indicating a mixed current with a decreased actual charging current. Intriguingly, the reduced front propagation velocities post-OER are also the same, regardless of the phase front position or direction of propagation. That the phase front shape and width seamlessly translate along the sample, and the front propagates at similar velocities for multiple sections and directions, shows that far from being affected by local variations, the phase front dynamics is rather governed by the effective media of the electrochemical system, and points to a degree of self-organizing behavior on a macroscopic scale far larger than the size of the particles within the electrode.

With time, both the charged and uncharged parts become gradually darker, revealing a small but observable uniform charging component.[41] Indeed, the near-uncharged sides, shown on the right side of the transition regions, become darker by similar amounts for all three cuts in Fig. 3(a)–(c). Such uniform charging component, superimposed with nonuniform charging by front propagation, was observed for several electrodes, thus ruling out spurious artifacts associated with specific samples. SI Section S7 shows another example demonstrating all the key results described above, based on a different sample (SIL4) and more quantitative fitting-based time-resolved analysis of the front propagation and uniform charging components.

To our knowledge, lateral phase front propagation along the *x*–*y* plane of the electrode, perpendicularly to the *z* direction of the applied electric field, has never been reported before in a charging electrode. We observed lateral front propagation in 6 different electrodes (summarized in Table 1), deposited by SILAR and electrodeposition methods (4 and 2 electrodes, respectively), with $Ni(OH)_2$ thickness ranging from *ca.* 50 to 450 nm, during CV at scan rates of 0.33 to 5 mV s^{-1} and galvanostatic charging at current densities of 36 to 360 μA cm^{-2} (corresponding to *C*-rates of 8 to 80 h^{-1}, respectively). Examples of lateral front propagation in additional samples (to samples SIL1, SIL3 shown above) are presented in Fig. S2–S5 and the corresponding Videos S2–S4 and S6. Therefore, we conclude that this phenomenon is reproducible across different samples, at least for thin-film electrodes deposited on ITO- and FTO-coated glass substrates, as the ones studied in this work. We also note that the phenomenon may be

Table 1 Survey table for $Ni(OH)_2$ electrodes showing lateral front propagation

Sample	Substrate and deposition method	Sample conditioning	Electrochemical cell	Electrochemical measurements	Featured in	Other characterizations
SIL1	ITO substrate	After formation	Cappuccino cell	CV, 0.2–0.6 V *vs.* Hg/HgO, 5 mV s^{-1}	Figure 1(c) and Video S1	Figure S15
	SILAR 50 cycles	As-deposited[a]	Cappuccino cell	CV, 0.2—0.6 V *vs.* Hg/HgO, 5 mV s^{-1}	Video S7[a]	
SIL2	ITO substrate SILAR 50 cycles	After formation	Beaker cell	CV, 0.2–0.54 V *vs.* Hg/HgO, 1 mV s^{-1}	Figure S4 and Video S4	Figures S8–S11, S14, S16–S21 and Tables S3–S5
SIL3	ITO substrate SILAR 50 cycles	After formation	Cappuccino cell	GCD, 20 μA (71.4 μA cm^{-2})	Fig. 2 and 3, Video S5	—
SIL4	ITO substrate SILAR 50 cycles	As deposited	Cappuccino cell	GCD, 100 μA (357.1 μA cm^{-2})	Figure S5 and Video S6	Figures S7, S12, S13, S22–S25, Tables S1 and S2
ED1	FTO substrate Electrodeposition 0.4 mA cm^{-2} 15 min	As deposited	Cappuccino cell	CV, 0.2–0.55 V *vs.* Hg/HgO, 0.33 mV s^{-1}	Figure S2[b] and Video S2[b]	—
ED2	FTO substrate Electrodeposition 0.36 mA cm^{-2} 5 min	After one GCD cycle	Cappuccino cell	GCD, 10 μA (35.7 μA cm^{-2})	Figure S3 and Video S3	—

[a] Uniform charging without lateral front propagation. [b] Imaged in reflection mode, with the microscope facing the front of the sample (unlike the other electrodes that were imaged in transmission mode, with the microscope facing the backside of the sample).

dependent on sample conditioning and electrochemical cycling history. Lateral front propagation did not appear immediately for as-deposited samples (see Video S7), but rather after formation by extensive electrochemical cycling (Videos S1–S6). The fact that it was observed for different samples suggests that it plays an important role in the lifecycle of nickel (oxy)hydroxide electrodes, encompassing their complex properties.

While the initial nucleation of the phase front may be influenced by elusive electrode heterogeneities or system boundaries, the subsequent lateral front propagation and pattern evolution cannot be accounted for by an inherent, static heterogeneity in the electrode. Instead, the observed dynamics are consistent with nonlinear kinetic feedback that amplifies local fluctuations and leads to spontaneous symmetry breaking. Understanding the fundamental mechanism and key elements that promote lateral, macroscopic front propagation is essential for practical applications, since this phenomenon can induce premature oxygen evolution and thereby constrain the electrode's ability to reach its full charging capacity. To this end, we examine a potential root cause of phase front instability responsible for the observed macroscopic behavior.

Mechanism of phase front instability

The prevailing paradigm of electrochemical phase transitions in battery electrodes,[42,43] like Li_xFePO_4 and $Ni(OH)_2$,[16,30] is that they occur *via* phase displacement, where the front between charged and discharged phases propagates in the direction of the electrical driving force, as illustrated in Fig. 1(a) and (b). This paradigm emerged from observations within individual particles during cycling.[4–6] In stark contrast, our findings show a phase front that propagates laterally—perpendicularly to the applied electrical field (Fig. 1(c) and 2(b)). This unexpected behavior highlights an unknown void in the perception of these transitions. Here, we propose that the lateral symmetry-breaking of the phase front as it propagates through the electrode emerges from the interplay between the energy of mixing (which promotes phase separation) and long-range Coulombic forces, a mechanism analogous to that seen in other systems, such as polymers.[44,45] To reveal the involved mechanism, we devise a continuum phase-field model and numerically investigate the key principles leading to such a symmetry-breaking instability.

The model accounts for the distinct electrical properties of the $Ni(OH)_2$ and NiOOH phases as proton conductor and semi-metallic phases, respectively,[30,41] supported by surface photovoltage measurements of unoxidized and oxidized electrodes (SI Section 8, Fig. S27).[46,47] Upon charging, proton and electron fluxes are generated at the phase front and extracted at the electrode boundaries, as illustrated in Fig. 4. The choice of a continuum framework is justified by the optically visible millimeter scale of the phase front (Fig. 1(c) and 2(b)), far larger than the size of the individual particles within the electrode. The millimeter scale of the phase front indicates that the forces governing its dynamics act on a macroscopic scale, in contrast to previous studies that looked at phase front dynamics in the microscopic scale of the individual particles within the electrode.[12,13,48,49] Seeking a macroscopic force that could govern the phase front dynamics in our system, we conjecture that Coulomb's force is responsible for macroscopic

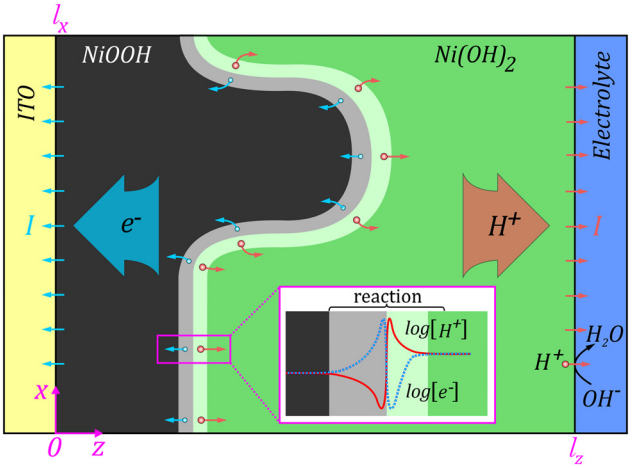

Fig. 4 Schematic illustration of the phase front instability through formation of a 'finger'-like feature during charging by an external current I, where the arrows indicate flux directions of electrons (left hand side) and protons (right hand side). The inset depicts typical electron and proton concentrations across the planar region of the phase front. The electrons and protons are created by the $Ni(OH)_2 \rightarrow NiOOH + H^+ + e^-$ reaction at the phase front. The corresponding model equations (eqn (1)) account for the spatiotemporal dynamics of the phase transition in the presence of Coulombic forces, in a domain $\Omega \in [l_z, l_x]$.

attraction or repulsion between locally charged regions along the $Ni(OH)_2$/NiOOH phase front.

We note that the proposed model is not intended to reproduce the experimental results, but rather to reveal a general mechanism that can explain the root cause of lateral front propagation. Complete modeling is considerably more complicated, as it would have to include specific processes at the electrode/electrolyte interface (*e.g.*, double layer effects,[50,51] the OER side reaction *etc.*) and at the electrode/current collector interface; additional phase transformations (*e.g.*, overcharging to the γ-NiOOH phase); dissolution–precipitation processes; spatial non-uniformities within the electrode (*e.g.*, thickness variations, impurity distribution *etc.*); edge effects that may influence the local ionic and electronic fluxes at the external boundaries of the electrode; iron accumulation that may influence the OER, and other effects. These effects are not accounted for in our model, and it should not be taken as a multiparameter complete system model but rather as a minimalistic—and thus robust—physical model that focuses on one key aspect of the phase transition, aiming to uncover the symmetry-breaking mechanism that drives lateral front propagation.

Before diving into the model, we first illustrate its key principles in Fig. 4. Galvanostatic charging drives the flux of electrons and protons from the $Ni(OH)_2$/NiOOH phase front to the ITO current collector and to the electrolyte, respectively. As a result, the NiOOH phase grows and the phase front propagates from the current collector towards the electrolyte. Like space charge regions in pn junctions at the boundary between p- and n-type semiconductors, as well as interfaces between ionic and electronic conductors,[52] here, too, a space charge region (SCR) is formed at the phase front between $Ni(OH)_2$, a proton conductor, and NiOOH, an electron conductor.[31] The SCR acts as a source of protons and electrons, generated by the charging reaction, and the rate of their generation depends on the external forces applied to the electrode (*i.e.*, the current) and on the intrinsic properties of those regions, akin to electron–hole generation in semiconductor pn junctions, *à la* the Shockley diode equation.[53] Consequently, the front propagation speed depends on the generation rate of protons and electrons (at the phase front) and on their transit times to the surface and current collector, respectively. The transit times depend on the proton and electron mobilities in the $Ni(OH)_2$ and NiOOH phases, respectively, the electric field, and the distance from the phase front to the surface (for the protons) and to the current collector (for the electrons). Since protons are much slower than electrons, we consider their transit time to the surface as the rate limiting step, and thus also as a major component in the symmetry breaking mechanism. If the proton transit time remains invariant on the location of the phase front, the front propagation would be insensitive to transverse perturbations, and the phase front would remain planar. However, if this is not the case, local perturbations in the charge density at the SCR along the phase front will be enhanced by coulombic forces between them, leading to instability of the planar phase front that may result in the formation of 'finger'-like features. This phenomenological mechanism reveals a general origin of the symmetry breaking mechanism that drives lateral front propagation, rooted solely in the physics of charged interfaces in semiconductors and mixed ionic–electronic conductors, and robust across a wide range of materials and model parameters.

The basic formulation of the model equations exploits the analogy between the donor–acceptor properties in bulk heterojunction organic photovoltaic (OPV) cells,[45] and the electron and proton conductivities of the NiOOH and $Ni(OH)_2$ phases in our system[30] These phases are prescribed by a standard Cahn–Hilliard-type order parameter, $u = \chi_{Ni(OH)_2} - \chi_{NiOOH}$, where $\chi_{Ni(OH)_2}$ and χ_{NiOOH} are the volume fractions of the respective phases. The order parameter obeys a double-well potential so that $u = 1$ corresponds to a fully discharged (reduced) $Ni(OH)_2$ electrode and $u = -1$ to a fully charged (oxidized) NiOOH electrode. The mobile charge carriers are protons (p) and electrons (n), generated at the NiOOH/$Ni(OH)_2$ phase front by the electrochemical charging reaction, $Ni(OH)_2 \rightarrow NiOOH + H^+ + e^-$; akin to the dissociation of excitons at donor–acceptor interfaces in OPV cells.[54] Finally, the system is complemented by Poisson's equation, and presented here in the form of dimensionless equations while referring the reader to SI Section S9 for the detailed derivation:

$$\frac{du}{dt} = -D_u \nabla \cdot J_u - 2k_f(1-u^2)\left(np\frac{1+u}{2} - \frac{1}{K}\frac{1-u}{2}\right), \quad (1a)$$

$$\frac{dn}{dt} = -D_n \nabla \cdot J_n - k_f(1-u^2)\left(np\frac{1+u}{2} - \frac{1}{K}\frac{1-u}{2}\right), \quad (1b)$$

$$\frac{dp}{dt} = -D_p \nabla \cdot J_p - \underbrace{k_f(1-u^2)\left(np\frac{1+u}{2} - \frac{1}{K}\frac{1-u}{2}\right)}_{Ni(OH)_2 \rightarrow NiOOH+H^+ + e^-}, \quad (1c)$$

$$-\varepsilon \nabla^2 \varphi = p - n, \quad (1d)$$

where n and p are the electron and proton concentrations, ε is the permittivity of the medium, and φ is the electrical potential. The respective fluxes are:

$$J_u(x,z) = -D_u\left[\nabla u + \zeta(1-u^2)\left(\nabla p(1+u) - \nabla n(1-u) + (p+n)\nabla u\right) + (1-u^2)(\beta W''\nabla u - \lambda \nabla^3 u)\right],$$

$$J_n(x,z) = -D_n[\nabla n - n\nabla\varphi - \zeta n(1-u)\nabla u],$$

$$J_p(x,z) = -D_p[\nabla p + p\nabla\varphi + \zeta p(1+u)\nabla u].$$

These fluxes are associated with the free energy of the system, where the transport coefficients satisfy $D_u \ll D_p < D_n$, and $k_f \ll K$ are the forward and equilibrium rates of the charging reaction, respectively. For other parameters see SI Section S9. We note that electron–proton generation, modeled by the $1 - u^2$ term in eqn (1), is localized at the phase front, and is negligible elsewhere.

The model equations are complemented by boundary conditions prescribing constant charge flux at the system boundaries at $z = 0$ and l_z (Fig. 4),

$$(J_u, J_n, J_p, \nabla\varphi)|_{z=0} = (0, -I, 0, 0), \quad (2a)$$
$$(J_u, J_n, J_p, \varphi)|_{z=l_z} = (0, 0, -I, 0),$$

where I represents the external current. In the lateral x direction the boundary conditions are periodic,

$$(u, n, p, \varphi)|_{x=0} = (u, n, p, \varphi)|_{x=l_x}. \quad (2b)$$

The potential at $z = l_z$ is pinned to preclude the translational invariance arising in Poisson's equation, as reported elsewhere.[45,55] We emphasize that while the model is semi-phenomenological, it is not limited to specific functional forms, *i.e.*, the formulation is flexible and allows physical refinement by demand. The above formulation provides a generic description of the basic physics through which the phase front instability mechanism can be uncovered (mathematically referred to phase fronts as heteroclinic connections in space). In what follows, we utilize numerical analysis since model complexity precludes analytical explorations.

We start by numerically solving eqn (1) for equilibrium conditions ($I = 0$), in which a steady front is formed near $z = 0$, as shown in Fig. 5(a) by profile $t = t_1 = 0$. Next, we compare the phase front propagation at two charging currents $I = 10^{-3}$ and 10^{-2} (presented by dashed and solid lines, respectively). The results, presented in Fig. 5(a), show that the space charge $\rho = p - n$ (the corresponding proton and electron density profiles are shown in Fig. S28) is localized at the phase front, for both currents. For the faster charging ($I = 10^{-2}$), the space charge decays during charging (profile $t = t_2$, solid line red curve), whereas for the slower charging ($I = 10^{-3}$) the space charge is preserved during charging (profile $t = t_2$, dotted line red curve). Since the average front propagation speed, s, depends on the flux of protons and electrons from the phase front region towards the surface ($z = l_z$) and current collector ($z = 0$), respectively (see inset in Fig. 5(a)), we find it informative to perform the comparison in terms of state-of-charge (SoC, the integrated charge $Q = I{\cdot}t$ normalized by the electrode's charge capacity) that is relative to the initial state (at $t = 0$),

$$\mathrm{SoC}(t) = \frac{1}{2l_x l_z}\left[1 + \int_\Omega \{u(t) - u(0)\}\mathrm{d}r\right],$$

where $\Omega \in [l_x, l_z]$ is the integration domain.

The salient difference between the space charge profiles at different charging rates ($I = 10^{-3}$ and 10^{-2}) is a direct result of the competition between the kinetics of the charging reaction at the phase front and the rate of charge transport of electrons and protons to the external boundaries (at $z = 0$ and l_z, respectively), similarly to the mechanism in OPV cells.[45] To validate the robustness of this behavior, we plot in Fig. 5(b) the progressive space charge decay for systems of different electrode thicknesses ($l_z = 20$ and 40, black and magenta curves, respectively) and see qualitatively similar results: stable space charge during fast charging and space charge decay during slow charging, presented by the dotted

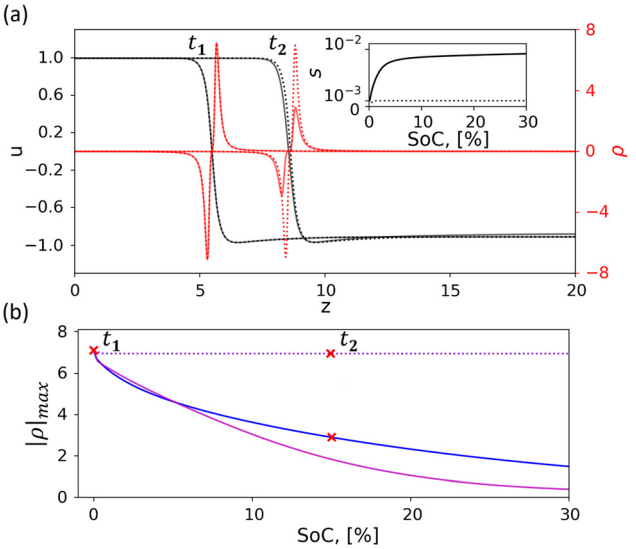

Fig. 5 Phase front dynamics and charge decay. Direct numerical integration of our model system equations (eqn (1)) and boundary conditions (eqn (2)) in one dimension (1D), showing the decay of generated charge at the NiOOH/Ni(OH)$_2$ phase front. (a) Selected profiles for the order parameter u (left y-axis, black curves) and the space charge ρ (right y-axis, red curves) for $l_z = 20$, and $I = 10^{-3}$ (solid line) and $I = 10^{-2}$ (dotted line), where $t_1 = 0$ corresponds to SoC = 0%, and t_2 to SoC = 15% ($t_2 = 3168$ for $I = 10^{-3}$ and 409 for $I = 10^{-2}$). The inset shows the average front propagation speed, s, as a function of SoC. (b) Demonstration of qualitatively similar charge decay, plotted in terms of maximal peak charge, $|\rho|_{max}$, as a function of SoC, for $l_z = 20$ and 40 (blue and magenta curves, respectively), and $I = 10^{-3}$ and 10^{-2} (solid and dotted lines, respectively). The blue and magenta dotted line curves overlap with each other.

and solid line curves, respectively. We also note that similar results are obtained for other parameter variations.

After uncovering the difference between slow and fast charging in 1D, we proceed to 2D simulations and examine the phase front instability to transverse perturbations. An initial sinusoidal perturbation is imposed to the phase front at $t = t_1 = 0$ (SoC = 0%), in common to both charging rates, $I = 10^{-3}$ and 10^{-2}, as shown in the order parameter maps in Fig. 6(a) and (e), respectively. The progression of this initial perturbation during charging is presented in Fig. 6(b), (c) and 6(f), (g) for different charging times that correspond to equal SoC values of 11% and 26% for slow and fast charging ($I = 10^{-3}$ and 10^{-2}, respectively). The planar phase front (*i.e.*, the interface between the green and black regions in the color maps) shows an instability in case of slow charging (Fig. 6(c)), whereas in case of fast charging it remains intact (Fig. 6(g)). As expected from the phase separation process, the instability favors the formation of large domains, as opposed to finite wavelength fingers in dissipative systems.[56]

From these model simulations, we deduce that the phase front instability is rooted in positive feedback caused by the sensitivity of interfacial space charge perturbations at the phase front region to the distance from the external boundaries, *i.e.*, the electrode surface and the ITO current collector, that extract the protons and electrons generated at the phase front. Thus, segments along the phase front that are closer to the surface become depleted of protons faster than other segments that are closer to the current collector, and *vice versa* for the electrons. This depletion results in the formation of regions with net negative and positive space charges, along the phase front, illustrated by – and + signs in Fig. 6(c). This asymmetry leads to counter-propagating phase fronts in the transverse and lateral directions, induced by the external field applied to the electrode and internal local fields that emerge from the charged regions along the phase front, respectively. As a result, the initial perturbation is enhanced, as shown in Fig. 6(c). The instability that forms negative and positive charged regions along the phase front diminishes at fast charging rates (Fig. 6(g)) whereby both protons and electrons are extracted at equal rates from everywhere along the phase front.

To illustrate the symmetry-breaking by the above positive feedback mechanism, we take two vertical cross-sections (along the z direction) at the apex and valley points of the black colored NiOOH phase, marked by the cyan and red vertical lines in Fig. 6(c) and (g), and plot the space charge profiles along these line scans in Fig. 6(d) and (h), respectively. For the slower charging case ($I = 10^{-3}$, Fig. 6(d)) we see that the space charge regions across the phase front are not balanced, resulting in a net negatively charged region at the apex point and a net positively charged region at the valley point. These electrically charged regions, along the phase front, result in macroscopic coulombic forces that give rise to flow of electrons and protons in different directions other than the direction of the external field applied to the electrode, enhancing the initial perturbation and eventually leading to symmetry-breaking and lateral front propagation. In contrast to the slow charging case, the space charge regions are balanced in the fast-charging case ($I = 10^{-2}$, Fig. 6(h)) and charge neutrality is preserved along the phase front. Overall, we show that electrically charged regions along the phase front can provide a generic mechanism that plausibly leads to lateral symmetry-breaking of the $Ni(OH)_2$/NiOOH phase front as it propagates through the electrode during slow charging. This mechanism diminishes during fast charging.

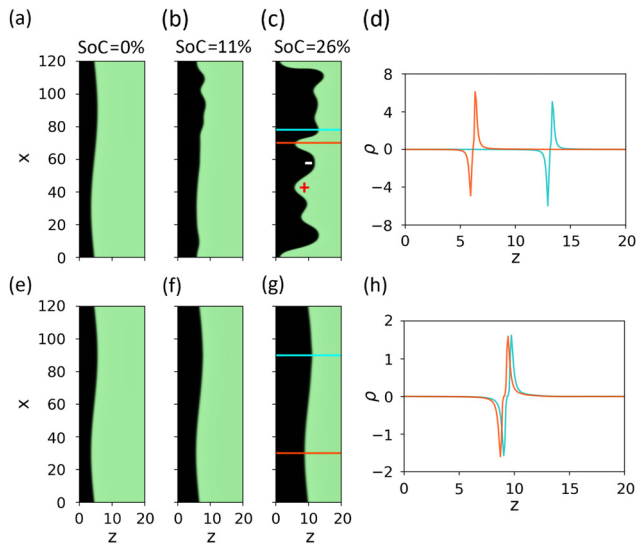

Fig. 6 Transverse phase front instability. Direct numerical integration of model system (eqn (1)) and boundary conditions (eqn (2)) in two dimensions (2D), demonstrating the transverse instability of the NiOOH/Ni$(OH)_2$ phase front for slow charging. (a)–(c) and (e)–(g) Color maps of the order parameter, u (green: $u = 1$, $Ni(OH)_2$; black: $u = -1$, NiOOH), at different times but identical SoC (0%, 11%, and 26%) for $I = 10^{-3}$ and $I = 10^{-2}$, respectively. (d), (h) Profiles of the space charge ρ along selected cross-sections corresponding to local apex and valley points (cyan and red, respectively) of the black colored phase (NiOOH, $u = -1$) in the order parameter maps in panels (c) and (g), respectively: (d) $I = 10^{-3}$; x = 70 and 78 (red and cyan curves); and (h) $I = 10^{-2}$; x = 30 and 90 (red and cyan curves).

Conclusions

Unprecedented lateral propagation, orthogonal to the applied electrical driving force, of a millimeter-scale phase front between charged NiOOH and discharged $Ni(OH)_2$ was observed by operando optical imaging during the charging of nickel (oxy)hydroxide thin-film electrodes. It led to nonuniform charging of the electrodes and premature oxygen evolution that constrains the ability to charge them to full capacity. The phenomenon was observed in both structurally uniform and nonuniform electrodes prepared by SILAR and electrochemical deposition methods, respectively, without any evidence relating it to possible structural or iron impurity nonuniformity in the electrode, suggesting a general phenomenon rather than sample-specific behavior.

To understand the spatiotemporal symmetry-breaking mechanism of this phenomenon, we devise a continuum

model and uncover generic positive feedback by long-range Coulomb forces between electrically charged regions along the phase front that drive planar front instability, akin to the governing mechanisms in bulk heterojunction organic photovoltaic (OPV) solar cells.[45] We exploit the model to explore rate dependence of the front instability, which may inform the design of dynamic cycling to improve electrode performance.[57]

The proposed mechanism is expected to advance the fundamental understanding of electrochemical phase transitions in battery electrodes by offering a fresh view on the role of long- and short-range forces on phase transitions during electrochemical cycling. Further studies will be needed to generalize these results from nickel (oxy)hydroxide thin-film electrodes on transparent conductive glass substrates, serving in this study as a model system for optical visualization of the phase transitions through the electrode, to other thin-film electrodes that are employed in solid state batteries[58] and to examine whether lateral instability persists in thick electrodes on porous substrates in conventional batteries.

Experimental

Chemicals

Double-distilled water (DDW) from a Direct-Q3 UV water purification system (Merck Millipore) was used for all solutions and cleaning processes (resistivity > 18.2 MΩ cm). Nickel sulfate heptahydrate (AR; Thermo Fisher Scientific) was used to prepare the $NiSO_4$ solution. 25% ammonium hydroxide (AR, Biolab) was used to prepare all NH_4OH-containing solutions. $Ni(NO_3)_2$ solutions were prepared with nickel nitrate hexahydrate powder 99.9% pure (Strem Chemicals). The electrolyte was prepared using AR-grade potassium hydroxide pearls (Gadot Chemicals). Detergent ES 7X (MP Company), acetone (AR; Biolab) and ethanol (AR; Biolab) were used for cleaning substrates before deposition.

Substrates

Indium tin oxide (ITO, 90 wt% In and 10 wt% Sn) coated float glass (sheet resistance of 8–12 ohms per square; Delta technologies), was used as transparent conductive substrates for preparing electrodes by SILAR deposition. Prior to $Ni(OH)_2$ deposition, the substrates were soaked in an ultrasonic bath for 10 min in each of the following solutions: detergent, DDW, ethanol and acetone. Then they were purged by N_2 gas (99.995%; Maxima), and plasma cleaned (Femto plasma cleaner, Diener Electronic) for 30 min at 100 W, 40 kHz, with O_2 gas (99.5%; Maxima) at a pressure of 0.4–0.6 mbar right before deposition.

Fluorinated tin oxide (FTO) coated soda-lime glass (TEC15 with sheet resistance of 12–15 ohms per square; Pilkington) was used as transparent conductive substrates for preparing electrodes by electrodeposition. Substrate cleaning and preparation prior to electrodeposition followed the procedure reported in ref. 59.

Successive ionic layer adsorption and reaction (SILAR) deposition

SILAR is a four-part deposition cycle which is repeated until the target thickness is achieved. It allows for the growth of uniform thin films, where the thickness is linearly correlated with the number of cycles.[37] Most of the electrodes reported in this study (Fig. 1–3, S4, S5, S17 and Videos S1, S4–S7) were prepared by SILAR deposition on ITO substrates by the following sequence (adapted from ref. 37):

I. 10 s immersion in the adsorption solution (1.55 wt% $NiSO_4$ and 4.05 wt% NH_4OH in DDW) to adsorb the $[Ni(NH_3)_n]^{2+}$ complex.

II. 5 s immersion in the rinsing solution (1.05 wt% NH_4OH in DDW) to remove weakly adsorbed cations from the surface, leaving only a monolayer of chemically adsorbed $[Ni(NH_3)_n]^{2+}$ cations.

III. 10 s immersion in the reaction solution (DDW) to react the $[Ni(NH_3)_n]^{2+}$ cations with hydroxide ions to produce the Ni $(OH)_2$ deposit (and NH_3 gas): $[Ni(NH_3)_n]^{2+}$ (ads) + $2OH^-$ (aq) → $Ni(OH)_2$ (s) + nNH_3 (g).

IV. 5 s immersion in the rinsing solution (1.05 wt% NH_4OH in DDW) to remove excess water.

10 to 50 of such SILAR cycles were repeated to yield $Ni(OH)_2$ layers of different thickness ranging from 3 to 51.7 nm (Table S3).

Electrodeposition

Electrodeposition of $Ni(OH)_2$ on FTO substrate was done in 0.1 M $Ni(NO_3)_2$ electrolyte at a temperature of 40 °C using a constant current of 4 mA over a submerged area of ~2.5 × 4 cm^2 (current density of 0.4 mA cm^{-2}) for 15 minutes for the sample shown in Fig. S2 and Video S2. Another sample was prepared by 5 min deposition at a current density of 0.36 mA cm^{-2} for the sample shown in Fig. S3 and Video S3.

Scanning electron microscopy (SEM)

The surface morphology of SILAR deposited $Ni(OH)_2$ electrode was examined before (bare ITO substrate) and after $Ni(OH)_2$ deposition (100 SILAR deposition cycles) by high-resolution scanning electron microscopy (HRSEM), using a Zeiss Ultra Plus field emission SEM. In the micrographs shown (Fig. S6), secondary electrons SE2 detector was used, the accelerating voltage was 3 kV and the beam current was 4 nA.

Atomic force microscopy (AFM)

The surface roughness of electrode SIL4 which showed lateral front propagation (Fig. S5 and Video S6) was measured by AFM before (bare ITO substrate) and after $Ni(OH)_2$ deposition (50 SILAR deposition cycles), and after formation by 200 CV cycles (0.2–0.54 V *vs.* Hg/HgO at 2 mV s^{-1}) in 1 M KOH electrolyte (Fig. S7 and Table S1), using Park Systems' XE 70 AFM operated in tapping mode with a 10 nm tip diameter AFM tip.

Transmission electron microscopy (TEM)

The microstructure of electrode SIL2 (50 SILAR deposition cycles) which showed lateral front propagation (Fig. S4 and Video S4) was examined, postmortem, by transmission electron microscopy (TEM). A cross-sectional lamella (Fig. S8) was cut out of the electrode by the standard lift out process using dual-beam focused ion beam (FEI Helios NanoLab G3 FIB) and placed on a molybdenum TEM grid. Prior to cutting the lamella, the electrode was

coated with GIS deposited tungsten to preserve the $Ni(OH)_2$ layer from possible ion milling damage in the FIB. The cross-sectional lamella was gently milled (Technoorg Linda's model IV8) and plasma cleaned (Fischione instruments' model 1020) before TEM measurements. High angle annular dark field scanning transmission electron microscopy (HAADF-STEM) imaging and energy dispersive spectroscopy (EDS) elemental mapping (Fig. S9), and high-resolution TEM (HRTEM) lattice imaging (Fig. S10) were carried out in a monochromated and double aberration-corrected (CEOS) Titan Cubed Themis G2 300 (FEI/Thermo Fisher) microscope operated at 300 kV. The resulting TEM images were analyzed with ImageJ software. Electron Energy Loss Spectroscopy (EELS) was performed in the 510–585 eV range (Fig. S11).

Rutherford backscattering spectrometry (RBS)

Chemical composition analysis and thickness estimation of SILAR electrodes, including SIL4 sample, were performed, postmortem, by RBS in a 1.7 MV tandem Pelletron particle accelerator (model 5SDH) using $^4He^+$ ion beam accelerated at 2.011 MV ± 1 KeV (Fig. S12, S13, and Table S2). The scattering angle was 169°. The RBS spectra were analyzed using Survey IBA DataFurnace software.

X-ray diffraction (XRD) and X-ray reflectometry (XRR)

Grazing incidence X-ray diffraction (GiXRD), at an angle of incidence of 0.2°, was used to probe the structure of sample SIL2 (Fig. S14), postmortem. The average thickness of sample SIL1 was measured using X-ray reflectometry (XRR) at an approximately 1° grazing angle (Fig. S15), with a beam footprint on the sample of $>2 \times 2$ mm^2. A Rigaku Smartlab diffractometer, operating with a Cu source at 9 kW, was used for the GiXRD and XRR measurements.

Spectroscopic reflectometry

The thickness of the $Ni(OH)_2$ layer in electrode SIL2 was measured, postmortem, at various spots (Fig. S16 and Table S3) using an S neox 3D optical profilometer (Sensofar Metrology). The spot size (diameter) was ~1 mm. To extract the $Ni(OH)_2$ layer thickness from the reflectometry spectra, a refractive index of 1.46 was assumed[60] within the wavelength measurement range of 600–700 nm. The undeposited bare ITO-coated glass substrate was used as the reference sample.

Time-of-flight secondary ion mass spectrometry (ToF-SIMS)

The impurity (particularly iron) distribution in electrode SIL2 was measured, postmortem, at various spots (Fig. S18 and Table S5) using IONTOF's ToF SIMS 5. At each spot, the composition was analyzed using 25 keV Bi^+ primary ions in positive ion mode over 50×50 μm^2. Depth profiling was performed by sputtering using 1 keV O_2^+ ions over an area of 400×400 μm^2 (cation analysis).

Operando optical imaging during electrochemical cycling

Most of the results were obtained using a "Cappuccino cell" designed for photoelectrochemical measurements[59] and used here for imaging the phase transition during electrochemical cycling. An 0.28 cm^2 round orifice defines the area of the working electrode in contact with the electrolyte, in front of a glass window that enables optical imaging through the nearly transparent electrode. The front and the back of the cell is optically transparent, with the sample acting as part of the back wall of the cell. The samples were sealed with a nitrile butadiene rubber (NBR) O-ring to prevent electrolyte leakage. In addition to the $Ni(OH)_2$ working electrode, a 5.0 cm long, 0.5 mm diameter platinum coil electrode (002233; ALS Co.) was used as a counter electrode, and an Hg/HgO electrode (RE-61AP; ALS Co.) was used as a reference electrode The cell was filled with 1 M KOH aqueous electrolyte (~10 ml).

A larger cell was used to characterize the larger SIL2 sample. This three-electrode cell comprises a 400 ml glass beaker with a Teflon cap holding the SIL2 working electrode, the platinum coil counter electrode (002233; ALS Co.) and the Hg/HgO reference electrode (RE-61AP; ALS Co.). All three electrodes are immersed in the beaker containing ~300 ml of 1 M KOH aqueous electrolyte.

Optical imaging through the electrode was video recorded by a Dino-Lite digital microscope (Model AM73915MZTL) operating at 20 frames per second at 1280 × 720 resolution. In most cases, the microscope was placed at the back of the cell (on the substrate side, not the electrolyte side), imaging the light being transmitted through the sample (electrodes SIL1–4, ED2). One sample, the thicker ED1 electrode, non-translucent in the oxidized state, was recorded in reflective mode with the microscope placed in the front of the cell. A white LED (GCS-6500-15; Mightex, operated at a current of 10 mA), diffused off of a white screen, provided illumination. The imaging setup is shown in Fig. S1. The optical data was recorded with DinoCapture 2.0 software (no gamma correction, default white balance, manual exposure, no back-illumination, WMV1 codec, Decoded format – Planar YUV 4:2:0) while the $Ni(OH)_2$ electrode was subjected to electrochemical cycling by cyclic voltammetry (CV) and galvanostatic charge and discharge (GCD) cycling using Ivium CompactStat potentiostat and IviumSoft software. Prior to operando imaging under electrochemical cycling, the electrode underwent formation with 200 CV cycles between 0.2 and 0.54 V *vs.* Hg/HgO to stabilize its capacity.

Optical data processing and analysis was performed with Python or MATLAB. For quantitative data analysis (SI Sections S7 and S8), the recorded video was converted to 8 bit grayscale format, with averaging each 10 frames to increase signal-to-noise ratio and then used to get a difference frame with respect to the discharged state of the electrode. The 20 pixel-width stripes, centered at the lines shown at Fig. 2(b) frame 3, were extracted from the difference video frames using the cubic spline interpolation. The 1D profiles were then extracted by averaging stripes along the normal-to-cut direction. The front position was evaluated as the maximum of the power spectrum for the orthogonal 1D Legendre polynomials basis functions of the degree 1–3 at pixel-centered kernel of size 71 pixel, mimicking the maxima of "noise-tolerant derivative".

Surface photovoltage spectroscopy (SPV)

SPV measurements were carried out to determine the electronic conductivity type of unoxidized and oxidized electrodes. The electrode was electrodeposited on a metallic Ni substrate and aged, and subsequently electrochemically oxidized as described in more detail in SI Section S8. A Kelvin probe (KP Technologies) with a 5 mm Ti probe and a hand held violet laser pointer were used for SPV measurements under ambient conditions in a dark enclosure. The probe was lowered until the gradient value in the software reached a value of 93 (arbitrary units, but qualitatively a measure of voltage amplitude per change in distance, which indicates how close to the sample the tip is). Although the tip could be brought closer, a sufficient gap between the tip and sample was required so that light could get through to the sample surface. After waiting several minutes for the contact potential difference (CPD) between tip and sample to reasonably stabilize, a hand held violet laser pointer (λ = 405 ± 10 nm, $P \approx 5$ mW) was directed to the sample position and turned on for about 6 minutes, holding it there before being turned off.

Author contributions

A. Y. and A. R. conceived the idea. A. K., A. B. S., and D. S. E. conducted the investigation, designed the experiments, performed the measurements and analysed the results. A. K., N. P., N. G. and A. Y. formulated the theoretical model. A. K. and A. Y. made the theoretical analysis and numerical simulations. A. K. and D. S. E. drafted the first manuscript. A. Y. and A. R. acquired the resources and supervised the research. All the authors discussed the results and commented on the manuscript, and A. K., A. B. S., D. S. E., A. Y., A. R. revised the manuscript.

Conflicts of interest

There are no conflicts to declare.

Data availability

The data supporting this article have been included in the Results and discussion section, the Experimental section, the supplementary videos, and as part of the supplementary information (SI). Supplementary information is available. See DOI: https://doi.org/10.1039/d6eb00045b.

Data are available upon request from the authors.

Acknowledgements

This research was supported by the Israel Science Foundation (grant no. 1224/21). The authors wish to thank Tasneem Shaaban of the Electrochemical Materials and Processes laboratory and Yossi Machpuda of the machine shop workshop at the Department of Materials Science and Engineering of the Technion for lab assistance and preparing customized labware for electrochemical measurements, respectively; Dr Galit Atiya and Dr Yaron Kauffmann of the Technion's Electron Microscopy Center for FIB cross-section sample preparation and TEM measurements, respectively; Dr Roman Kris for consulting on image processing aspects; Joanna Sklar of Prof. Boaz Pokroy's Bio-Inspired Surface Engineering and Biomineralization Lab at the Department of Materials Science and Engineering of the Technion for spectroscopic reflectometry measurements; Dr Olga Girshevitz of BINA's (Bar-Ilan Institute for Nanotechnology & Advanced Materials) Ion Beam Analysis (IBA) laboratory at Bar-Ilan University for RBS measurements; and Dr Shaul Michaelson of the Technion's Surface Science Laboratory for ToF-SIMS measurements. The authors acknowledge the financial and infrastructure support from the Israeli National Institute for Energy Storage (I-NIES), the Crown Vanguard Award for Science and Technology Fund, and the Nancy and Stephen Grand Technion Energy Program (GTEP). A. R. acknowledges the support of the L. Shirley Tark Chair in Science.

References

1 A. K. Padhi, K. S. Nanjundaswamy and J. B. Goodenough, *J. Electrochem. Soc.*, 1997, **144**, 1188–1194.
2 M. Tang, W. C. Carter and Y.-M. Chiang, *Annu. Rev. Mater. Res.*, 2010, **40**, 501–529.
3 K. Malaie, F. Scholz and U. Schröder, *ChemElectroChem*, 2023, **10**, e202201118.
4 A. Sood, A. D. Poletayev, D. A. Cogswell, P. M. Csernica, J. T. Mefford, D. Fraggedakis, M. F. Toney, A. M. Lindenberg, M. Z. Bazant and W. C. Chueh, *Nat. Rev. Mater.*, 2021, **6**, 847–867.
5 J. T. Mefford, A. R. Akbashev, M. Kang, C. L. Bentley, W. E. Gent, H. D. Deng, D. H. Alsem, Y.-S. Yu, N. J. Salmon, D. A. Shapiro, P. R. Unwin and W. C. Chueh, *Nature*, 2021, **593**, 67–73.
6 Y. Huang, B. Wang, F. Chen, Y. Han, W. Zhang, X. Wu, R. Li, Q. Jiang, X. Jia and R. Zhang, *Adv. Opt. Mater.*, 2022, **10**, 2101783.
7 M. D. Radin, S. Hy, M. Sina, C. Fang, H. Liu, J. Vinckeviciute, M. Zhang, M. S. Whittingham, Y. S. Meng and A. Van der Ven, *Adv. Energy Mater.*, 2017, **7**, 1602888.
8 H. Liu, F. C. Strobridge, O. J. Borkiewicz, K. M. Wiaderek, K. W. Chapman, P. J. Chupas and C. P. Grey, *Science*, 2014, **344**, 1252817.
9 C. Zeng, J. Liang, C. Cui, T. Zhai and H. Li, *Adv. Mater.*, 2022, **34**, 2200777.
10 Y. Wu and N. Liu, *Chem*, 2018, **4**, 438–465.
11 J. Lim, Y. Li, D. H. Alsem, H. So, S. C. Lee, P. Bai, D. A. Cogswell, X. Liu, N. Jin, Y. Yu, N. J. Salmon, D. A. Shapiro, M. Z. Bazant, T. Tyliszczak and W. C. Chueh, *Science*, 2016, **353**, 566–571.
12 Y. Li, H. Chen, K. Lim, H. D. Deng, J. Lim, D. Fraggedakis, P. M. Attia, S. C. Lee, N. Jin, J. Moškon, Z. Guan,

W. E. Gent, J. Hong, Y.-S. Yu, M. Gaberšček, M. S. Islam, M. Z. Bazant and W. C. Chueh, *Nat. Mater.*, 2018, **17**, 915–922.
13 J. Park, H. Zhao, S. D. Kang, K. Lim, C.-C. Chen, Y.-S. Yu, R. D. Braatz, D. A. Shapiro, J. Hong, M. F. Toney, M. Z. Bazant and W. C. Chueh, *Nat. Mater.*, 2021, **20**, 991–999.
14 W. Dreyer, J. Jamnik, C. Guhlke, R. Huth, J. Moškon and M. Gaberšček, *Nat. Mater.*, 2010, **9**, 448–453.
15 R. Malik, F. Zhou and G. Ceder, *Nat. Mater.*, 2011, **10**, 587–590.
16 M. Z. Bazant, *Acc. Chem. Res.*, 2013, **46**, 1144–1160.
17 M. Patzauer and K. Krischer, *Phys. Rev. Lett.*, 2021, **126**, 194101.
18 G. Ertl, *Angew. Chem., Int. Ed.*, 2008, **47**, 3524–3535.
19 A. Shukla, *J. Power Sources*, 2001, **100**, 125–148.
20 M. Chatenet, B. G. Pollet, D. R. Dekel, F. Dionigi, J. Deseure, P. Millet, R. D. Braatz, M. Z. Bazant, M. Eikerling, I. Staffell, P. Balcombe, Y. Shao-Horn and H. Schäfer, *Chem. Soc. Rev.*, 2022, **51**, 4583–4762.
21 G. Ruan, F. Todman, G. Yogev, R. Arad, T. Smolinka, J. O. Jensen, M. D. Symes and A. Rothschild, *Nat. Rev. Clean Technol.*, 2025, **1**, 380–395.
22 L. Zhang, D. Shi, T. Liu, M. Jaroniec and J. Yu, *Mater. Today*, 2019, **25**, 35–65.
23 G. A. Niklasson and C. G. Granqvist, *J. Mater. Chem.*, 2007, **17**, 127–156.
24 M. K. Carpenter, R. S. Conell and D. A. Corrigan, *Sol. Energy Mater.*, 1987, **16**, 333–346.
25 O. Glemser and J. Einerhand, *Z. Anorg. Chem.*, 1950, **261**, 43–51.
26 O. Glemser and J. Einerhand, *Z. Anorg. Chem.*, 1950, **261**, 26–42.
27 B. E. Conway and P. L. Bourgault, *Can. J. Chem.*, 1962, **40**, 1690–1707.
28 H. Bode, K. Dehmelt and J. Witte, *Electrochim. Acta*, 1966, **11**, 1079–1087.
29 G. W. D. Briggs and M. Fleischmann, *Trans. Faraday Soc.*, 1971, **67**, 2397.
30 R. Huggins, H. Prinz, M. Wohlfahrtmehrens, L. Jorissen and W. Witchel, *Solid State Ionics*, 1994, **70–71**, 417–424.
31 F. Dionigi and P. Strasser, *Adv. Energy Mater.*, 2016, **6**, 1600621.
32 L. Trotochaud, S. L. Young, J. K. Ranney and S. W. Boettcher, *J. Am. Chem. Soc.*, 2014, **136**, 6744–6753.
33 N. Hayek, A. Landman, Y. Halpern, I. Slobodkin, E. S. Davydova and A. Rothschild, *J. Mater. Chem. A*, 2022, **10**, 726–739.
34 A. Landman, S. Hadash, G. E. Shter, A. Ben-Azaria, H. Dotan, A. Rothschild and G. S. Grader, *Adv. Funct. Mater.*, 2021, **31**, 2008118.
35 R. Barnard, G. T. Crickmore, J. A. Lee and F. L. Tye, *J. Appl. Electrochem.*, 1980, **10**, 61–70.
36 P. Zhang, M. Ding, X. Li, C. Li, Z. Li and L. Yin, *Adv. Energy Mater.*, 2020, **10**, 2001789.
37 J. Liu, S. Y. Chiam, J. Pan, L. M. Wong, S. F. Y. Li and Y. Ren, *Sol. Energy Mater. Sol. Cells*, 2018, **185**, 318–324.
38 S. Klaus, Y. Cai, M. W. Louie, L. Trotochaud and A. T. Bell, *J. Phys. Chem. C*, 2015, **119**, 7243–7254.
39 D. A. Corrigan, *J. Electrochem. Soc.*, 1987, **134**, 377–384.
40 V. Srinivasan, J. W. Weidner and J. Newman, *J. Electrochem. Soc.*, 2001, **148**, A969.
41 R. Barnard, C. F. Randell and F. L. Tye, *J. Appl. Electrochem.*, 1980, **10**, 109–125.
42 X. Lu, M. Lagnoni, A. Bertei, S. Das, R. E. Owen, Q. Li, K. O'Regan, A. Wade, D. P. Finegan, E. Kendrick, M. Z. Bazant, D. J. L. Brett and P. R. Shearing, *Nat. Commun.*, 2023, **14**, 5127.
43 M. Z. Bazant, *Faraday Discuss.*, 2023, **246**, 60–124.
44 R. Choksi, M. A. Peletier and J. F. Williams, *SIAM J. Appl. Math.*, 2009, **69**, 1712–1738.
45 A. Z. Shapira, N. Gavish and A. Yochelis, *EPL*, 2019, **125**, 38001.
46 L. Kronik and Y. Shapira, *Surf. Sci. Rep.*, 1999, **37**, 1–206.
47 A. Kay, D. A. Grave, D. S. Ellis, H. Dotan and A. Rothschild, *ACS Energy Lett.*, 2016, **1**, 827–833.
48 N. Clarke and G. A. Buxton, *Soft Matter*, 2024, **20**, 1651–1656.
49 E. Avalos, T. Teramoto, Y. Hirai, H. Yabu and Y. Nishiura, *ACS Omega*, 2024, **9**, 17276–17288.
50 M. Becker, P. Loche, M. Rezaei, A. Wolde-Kidan, Y. Uematsu, R. R. Netz and D. J. Bonthuis, *Chem. Rev.*, 2024, **124**, 1–26.
51 J. Huang, S. Chen and M. Eikerling, *J. Chem. Theory Comput.*, 2021, **17**, 2417–2430.
52 C. Xiao, H. Wang, R. Usiskin, P. A. van Aken and J. Maier, *Science*, 2024, **386**, 407–413.
53 W. Shockley, *Bell Syst. Tech. J.*, 1949, **28**, 435–489.
54 G. A. Buxton and N. Clarke, *Phys. Rev. B: Condens. Matter Mater. Phys.*, 2006, **74**, 085207.
55 A. Z. Shapira, N. Gavish, H. Uecker and A. Yochelis, *Phys. Rev. E*, 2020, **102**, 062213.
56 A. Hagberg, A. Yochelis, H. Yizhaq, C. Elphick, L. Pismen and E. Meron, *Phys. D*, 2006, **217**, 186–192.
57 A. Geslin, L. Xu, D. Ganapathi, K. Moy, W. C. Chueh and S. Onori, *Nat. Energy*, 2025, **10**, 172–180.
58 S. Lobe, A. Bauer, S. Uhlenbruck and D. Fattakhova-Rohlfing, *Adv. Sci.*, 2021, **8**, 2002044.
59 K. D. Malviya, H. Dotan, K. R. Yoon, I. D. Kim and A. Rothschild, *J. Mater. Res.*, 2016, **31**, 1565–1573.
60 W. Visscher, *J. Phys. Colloques*, 1983, **44**, C10-213–C10-216, DOI: 10.1051/jphyscol:19831044.